

## ARTICLE

# Order of Magnitude Increase in Photocatalytic Rate for Hierarchically Porous Anatase Thin Films Synthesized from Zinc Titanate Coatings

Cite this: DOI: 10.1039/x0xx00000x

Nathanya J. Platt,<sup>a</sup> Karl M. Kaye,<sup>a</sup> Gregory J. Limburn,<sup>a</sup> Samuel D. Cosham,<sup>a</sup> Alexander N. Kulak,<sup>b</sup> Robert G. Palgrave,<sup>c</sup> Geoffrey Hyett<sup>a\*</sup>

Received 00th January 2012,

Accepted 00th January 2012

DOI: 10.1039/x0xx00000x

[www.rsc.org/](http://www.rsc.org/)

In this paper we report on the use of aerosol assisted chemical vapour deposition (AACVD) to form thin films of the zinc titanate phases using zinc acetate and titanium isopropoxide as precursors in methanol solution. Analysis by XRD and XPS found that through variation in experimental conditions we have been able to synthesize films of zinc titanate with composition of  $\text{Zn}_2\text{TiO}_4$  or  $\text{Zn}_{0.3}\text{Ti}_{2.7}\text{O}_{4.94}$ , which adopt the spinel and pseudobrookite structure respectively. In addition, we have also formed hybrid films of  $\text{Zn}_2\text{TiO}_4$  with either  $\text{ZnTiO}_3$  or  $\text{ZnO}$ . Using a technique previously reported with powders, the mixed  $\text{ZnO}$  and  $\text{Zn}_2\text{TiO}_4$  films were treated with acid to produce porous  $\text{Zn}_2\text{TiO}_4$  which, through reduction and vapour leaching of zinc, were converted to hierarchically porous thin films of anatase  $\text{TiO}_2$ . This conversion was monitored by XRD. Analysis of photocatalytic activity of the hierarchically porous titania, using dye and stearic acid degradation tests, found a factor of 12 to 14 increase in rates of photocatalysis over conventional  $\text{TiO}_2$  thin films. Finally we are able to report a maximum formal quantum efficiency for stearic acid degradation of  $1.76 \times 10^{-3}$  molecules per photon.

## Introduction

As a material with low cost and low toxicity, titanium dioxide is one of the most widely investigated semiconductor UV photocatalysts, and has found application in self-cleaning glazing, wastewater treatment, and anti-microbial coatings.<sup>1-4</sup> The self-cleaning properties of titanium dioxide derive from its ability to photocatalyse, at room temperature, the reaction of organic species with atmospheric oxygen to form carbon dioxide, water and mineral acids.<sup>5</sup> However, when considering titanium dioxide for wastewater treatment there is a long-standing debate about the most appropriate microstructure or support for the catalyst.<sup>6</sup> Opinion on this matter can be divided into two broad categories: should the catalyst be dispersed or immobilized? In the first case, the photocatalyst is dispersed as a powder slurry in the aqueous wastewater medium, maximizing the contact between the catalyst and the solution. This approach also has the advantage of the relative ease and low cost of the synthesis of titanium dioxide powders or nanoparticles.<sup>7-8</sup> However, in slurry systems there are concerns about ensuring even light exposure for the photocatalyst, and more crucially a method is required for the separation of the catalyst and the treated water, which can complicate the implementation and prevent the photocatalyst being used in a continuous flow system. In contrast, in immobilized systems

the photocatalyst is secured to a substrate. This can lead to a reduction in the contact area between the photocatalyst and the medium, but does allow for use in flow systems, and removes the need for a separation step. Common implementations include packed-bed reactors, microfluidic systems and films.<sup>6,9</sup> A further advantage is that such immobilized systems can also be used for self-cleaning surfaces and in the treatment of air for the removal of volatile organic compounds (VOCs) and nitrogen oxide ( $\text{NO}_x$ ) pollution.<sup>10-11</sup>

Attempts have been made to combine the advantages of immobilized systems with the high surface area of dispersed systems through the use of hierarchically porous catalysts. These are materials with pores or networks of channels on at least two different length scales, typically mesopores and macropores. The small scale pores increase the surface area, while the larger ones maximize mass transport. Hierarchically porous titania powders have been synthesized by a number of routes including freeze-drying,<sup>12</sup> biomimetic protein templating,<sup>13</sup> and sol-gel templating routes,<sup>14-15</sup> a recent review by Coppens et al. provides an excellent summary.<sup>16</sup> Due to their porosity, these powders have high surface area and, unsurprisingly, this also leads to significant increases in photocatalytic rates.<sup>12</sup> The introduction of hierarchical porosity into an adherent thin film for use as a heterogeneous immobilized photocatalyst is more challenging, but has been

successfully achieved using templated sol-gel dip coating routes.<sup>15,17-18</sup> The porosity introduced into these films led to increases in accessible surface and resulted in three- to seven-fold increases in photocatalytic rates compared to non-porous samples. These results highlight the benefits of hierarchically porous thin films, but the sol-gel route used is a complex batch process requiring templating, which limits the potential for use in low cost, large scale applications.

In contrast, Seshadri and co-workers have established an innovative, template-free route for the introduction of porosity into inorganic materials, through selective vapour phase leaching.<sup>19-21</sup> They have extended this work to include spontaneous compositional change in mixed metal oxide materials and, of particular interest from the point of view of photocatalysis, this includes work on hierarchically porous titanium dioxide powders.<sup>21</sup> Their method started with a sintered mixture of ZnO and Zn<sub>2</sub>TiO<sub>4</sub>, from which the zinc oxide was removed using acid leaching to leave interconnected pores of 2-5 μm diameter in a Zn<sub>2</sub>TiO<sub>4</sub> matrix. The zinc titanate was then thermally decomposed into a mixture of fine grained ZnO and TiO<sub>2</sub>, while retaining the macropore network. Removal of the spontaneously formed zinc oxide using vapour phase leaching introduced pores of 100-200 nm into the remaining titania network, which alongside the macropore network gave the sample the desired hierarchical porosity.<sup>21</sup> In this work we propose that this template-free route could be applied to thin films formed using chemical vapour deposition (CVD). This would allow us to combine the benefits of high surface area and good mass transport found in hierarchically porous materials with the ability of CVD to inexpensively form adherent films on a large scale.<sup>22</sup>

To utilize this strategy a thin film comprising a mixture of zinc oxide and zinc titanate is required, synthesized using CVD. Separate routes to zinc oxide and titanium dioxide are widely reported – both systems have been extensively investigated as thin films using CVD synthesis, however the ternary zinc-titanium-oxide system is less well explored in the form of thin films. Conventional solid state chemistry has identified four stable compositions in the Zn-Ti-O system. The most common is Zn<sub>2</sub>TiO<sub>4</sub> which adopts the inverse spinel structure with both the typical cubic form and a tetragonal distortion.<sup>23</sup> Related to this is the more titanium-rich zinc titanate phase, Zn<sub>2</sub>Ti<sub>3</sub>O<sub>8</sub>, which also adopts a cubic spinel structure, but with zinc found only on the tetrahedral sites and titanium occupying ¾ of the normal spinel octahedral sites. These two cubic spinel zinc titanates have similar diffraction patterns, but can be distinguished by the smaller lattice parameter of the more titanium-rich Zn<sub>2</sub>Ti<sub>3</sub>O<sub>8</sub> of 8.40 Å, leading to a slight shift in the position of the Bragg peaks compared to the pattern of Zn<sub>2</sub>TiO<sub>4</sub> with a lattice parameter of 8.47 Å.<sup>23-25</sup> In addition to these compositions, ZnTiO<sub>3</sub> has been reported,<sup>24</sup> taking the rhombohedral ilmenite structure, and most recently a zinc titanate with the pseudobrookite structure has been found, Zn<sub>0.61</sub>Ti<sub>2.39</sub>O<sub>4.94</sub>; the only stable zinc titanate where titanium is not found in its maximum oxidation state.<sup>26</sup>

As thin films, both ZnTiO<sub>3</sub> and Zn<sub>2</sub>TiO<sub>4</sub> have been synthesized using magnetron sputtering and via sol-gel routes.<sup>27-30</sup> A sol-gel route has also been used to produce hybrid films of ZnO and Zn<sub>2</sub>TiO<sub>4</sub>.<sup>31-32</sup> To our knowledge, however, there has been only one report on the use of CVD for the deposition of a zinc titanate film. Chen *et al.* used MOCVD of titanium tetraisopropoxide, diethyl zinc and water to form amorphous films, which required annealing at 650 °C to form a crystalline film of Zn<sub>2</sub>TiO<sub>4</sub>.<sup>33</sup>

In this paper we will make use of aerosol assisted chemical vapour deposition (AACVD) to form thin films of the zinc titanate phases.<sup>34</sup> It has been previously shown that AACVD can be used to independently synthesize films of zinc oxide from zinc acetate, and titanium dioxide using titanium isopropoxide, both in methanol solution.<sup>35-36</sup> In this work, we will show that by combining both precursors in a single solution in different ratios, it is possible to form films containing all of the known structures of zinc titanate, and crucially also films containing both zinc titanate and zinc oxide. We subsequently show that these mixed ZnO-Zn<sub>2</sub>TiO<sub>4</sub> films can be successfully converted into hierarchically porous thin films of TiO<sub>2</sub> while retaining adhesion and with an increase in accessible surface area. Photocatalytic testing of these films show a greater than one order of magnitude increase in photocatalytic activity, compared to conventional non-porous films, and highlights the enormous potential of these films for self-cleaning applications.

## Experimental Methods

**Thin film synthesis.** Thin films were deposited by AACVD using a simple hot-wall reactor, consisting of a silica tube (35 mm diameter, 600 mm length, Robson Scientific) placed in a 300 mm tube furnace (Carbolite), which provided the external heat source for the deposition. The substrates used were silica coated float glass of dimensions 25 × 150 × 3.2 mm<sup>3</sup> (Pilkington NSG), which were placed in the silica tube on top of a semi-circular section carbon block (25 mm diameter, 150 mm length, Olmec) which acted as a support and also a thermal mass to allow more rapid and even heating of the substrate, regulating the deposition temperature.

The precursor solution was held in a 100 ml three necked round bottom flask, partially submerged in a water-filled 600 ml crystallizing dish containing a piezoelectric humidifier (Maplin, product no. L38AK). When the flask was positioned above the humidifier it generated a mist of the precursor solution which was transported using a flow of argon gas, controlled by a rotameter, to the reactor. The exhaust passed through a silicone oil bubbler to prevent back diffusion of air into the reactor.

For all depositions, zinc (II) acetate (Sigma Aldrich, 99.99%) and titanium (IV) isopropoxide (Sigma Aldrich, 99.999%) were used as the zinc and titanium precursors, dissolved in 40 ml of methanol (Fisher Scientific, Technical Grade). Reactions were carried out with a carrier gas flow of 0.8 L min<sup>-1</sup> of argon (BOC, Pureshield) and with a substrate

deposition temperature of 450 °C. In each experiment the amount of the two precursors was varied to control the molar ratio of titanium to zinc supplied *via* the precursor aerosol, but such that the sum of both metal precursors was maintained at approximately  $2.25 \times 10^{-3}$  mol. The zinc acetate mass was determined using a Mettler Toledo microbalance, while the volume of titanium isopropoxide used was determined using a Fisherbrand Elite 100-1000  $\mu$ l single-channel auto-pipette.

**Post synthesis treatment of films.** Using the above synthetic route, a sample of film composed of a mixture of ZnO and  $\text{Zn}_2\text{TiO}_4$  was identified, and a section of approximate dimensions  $20 \times 25 \times 3.2 \text{ mm}^3$  was treated for conversion to  $\text{TiO}_2$ . In the first step the zinc oxide was removed by submerging the sample for 1 hour in an aqueous solution of 0.054 M ethanoic acid. The acid treated film of  $\text{Zn}_2\text{TiO}_4$  and an additional, as-made film of  $\text{Zn}_2\text{TiO}_4$  were then placed on a carbon block in an alumina tube in a furnace and heated to 575 °C under a steady flow of 5%  $\text{H}_2$  in  $\text{N}_2$  gas (BOC) for 72 hours. This temperature was chosen as the highest sustainable before the float glass substrates will begin to soften, but at which it was observed that the zinc could be reduced and lost from the sample under its own vapour pressure.

**X-ray diffraction.** Grazing incident X-ray diffraction patterns were collected from the samples in the range  $10 < 2\theta < 70^\circ$  using a Rigaku Smart Lab diffractometer equipped with a rotating anode  $\text{Cu K}\alpha$  radiation source (45 kV, 200 mA). Grazing incident (GI) scans were collected using a  $2^\circ$  incident angle, preventing over-penetration of the beam into the sample, and modelled using the GSAS suite of software packages, with the EXPGUI graphical interface.<sup>37-38</sup> It was necessary to make use of a preferred orientation model for many of the phases, to account for the crystallite alignment which is common in thin films.<sup>39</sup> These limitations meant that the majority of the structural parameters could not be refined, but phase fraction values could be determined – albeit with lower accuracy than is possible with more standard powder diffraction data.

**XPS details.** X-ray photoelectron spectroscopy (XPS) was carried out on a Thermo Fisher Scientific K-Alpha instrument, using  $\text{Al K}\alpha$  radiation (1486.6 eV) and operated in constant analyser energy mode. Samples were introduced into the vacuum chamber held at a base pressure of  $5 \times 10^{-9}$  mbar, and the incident X-ray beam focused to a 400 micron spot at the sample surface, which defined the analysis area. Survey spectra and high resolution spectra were taken with pass energies of 200 eV and 50 eV respectively. Charge neutralization was carried out using a dual beam  $\text{Ar}^+$  and electron flood gun. Charge correction of spectra was carried out using the adventitious C1s, which was set to a binding energy of 284.6 eV. Etching was carried out using a 3 keV  $\text{Ar}^+$  ion source, rastered over an area of  $4 \text{ mm}^2$ , considerably larger than the analysis area ensuring that the signal after ion etching came only from the base of the crater. After etching, the adventitious carbon was removed, so no charge correction was carried out, therefore absolute peak binding energies post etching are considered unreliable and not reported here.

**SEM imaging.** A FEI Nova 450 FEG-SEM, operating at 3 kV in secondary electron mode with a ETD detector was used to collect SEM images, at a working distance of 5 mm. All samples were coated with 10 nm of gold, deposited by sputter coating.

**Photocatalytic testing.** Two methods for assessing photocatalytic activity were used in this work. Both made use of a UV light source (CIF, supplied by RS) equipped with  $4 \times 8$  W BLB bulbs arranged in parallel in an exposure box. These lamps provide a peak output of photons with a wavelength of 365 nm. The intensity of UV light reaching the sample in each experiment was measured using a radiometer photometer (ILT1400 equipped with a SEL623 probe).

The first test was photocatalytic reduction of an indicator ink, dichloroindophenol (DCIP), which undergoes a blue to colourless two electron reduction in the presence of an activated photocatalyst and a sacrificial electron donor, which in this case was glycerol.<sup>40</sup> In the procedure, test samples of approximate area  $25 \times 15 \text{ mm}^2$  were placed in an 80 ml crystallizing dish with 25 ml of a solution of DCIP ( $5.22 \times 10^{-5}$  M) and glycerol ( $1.26 \times 10^{-3}$  M) – a volume sufficient to just cover the film, and which was stirred throughout the reaction. The UV light source was suspended above the test dish at a distance of 50 mm, giving a measured light intensity of  $4.0 \text{ mWcm}^{-2}$ . The dye solution was allowed to come to equilibrium in the dark for 60 mins, then sampled at intervals of 30 mins of UV irradiation. Sampling was carried out by removing a 3.5 ml aliquot of the solution, recording the absorption spectrum in the range of 400-800 nm, using a Lambda 750S spectrometer (Perkin Elmer), and then returning the aliquot to the test solution to maintain overall volume.

The second photocatalytic test used was the degradation of stearic acid by a photocatalyst under UV irradiation.<sup>41</sup> The procedure was conducted on the same samples used in the dye degradation test. Dip coating was used to deposit a thin layer of stearic acid from a 0.005 M solution of the acid in dichloromethane. The samples were then masked by an aluminium plate to expose a circle of 10 mm diameter with the plate also being used as the sample holder for the spectrometer, allowing consistent light exposure and placement during sampling. Samples were placed directly onto the light box exposure surface, giving an irradiation intensity of  $5.6 \text{ mWcm}^{-2}$ , or approximately  $1.0 \times 10^{16}$  photons  $\text{s}^{-1} \text{ cm}^{-2}$ . Transmission IR spectra were recorded using a Perkin Elmer Spectrum 100 FTIR at 5 min intervals for 30 mins, and at 10 mins intervals thereafter, over the range of 3000-2800  $\text{cm}^{-1}$  where the principal C-H stretches of stearic acid are found. Integration of the area of the peaks found in this range allows quantification of the amount stearic acid on the surface of the film, calculated using the relationship previously published in the literature that  $1 \text{ cm}^{-1}$  of integrated area is equivalent to  $9.7 \times 10^{15}$  molecules of stearic acid.<sup>42</sup>

**Accessible surface area.** The absorption of methylene blue dye onto and into the films was used to determine the

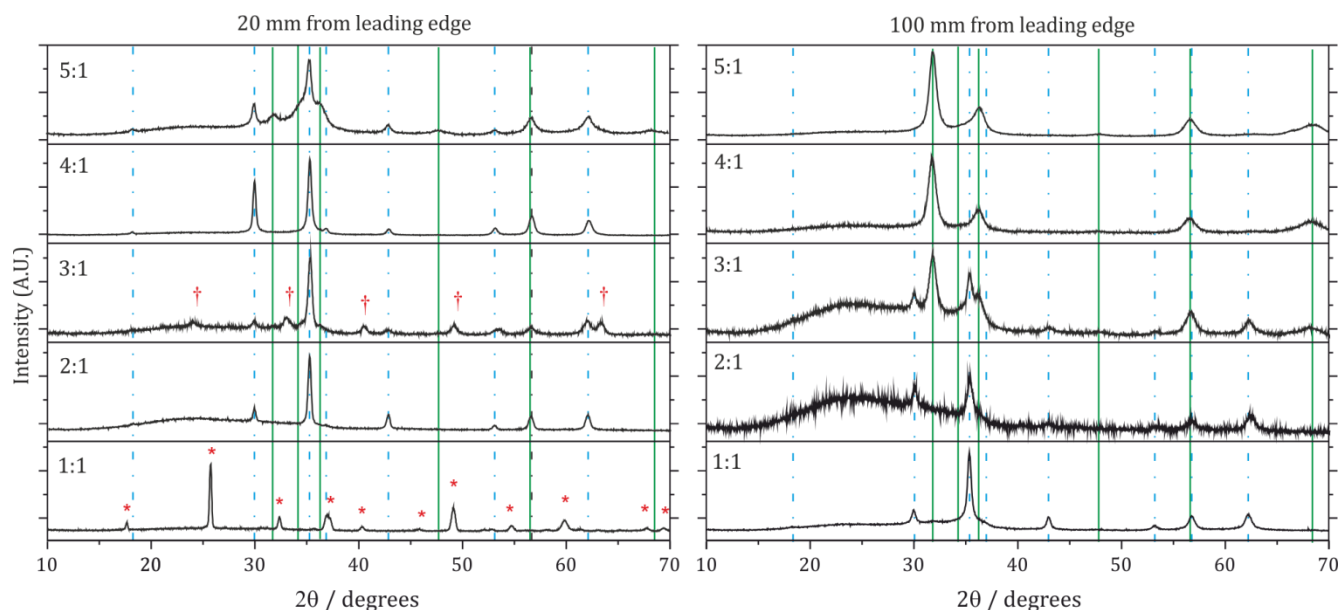


**Figure 1.** Diffraction patterns collected at front (20 mm) and rear (100 mm) sections of films synthesized with ratios of zinc acetate to titanium isopropoxide from 1:1 to 5:1. The broken blue lines represented the positions of the peaks for  $\text{Zn}_2\text{TiO}_4$ , while the solid green lines those for ZnO. The front pattern for the 1:1 film contains peaks that can be indexed to  $(\text{ZnTi})_3\text{O}_5$ , marked with a red asterisk (\*). The front section of the 3:1 film contains peaks which can be indexed to  $\text{ZnTiO}_3$ , marked with a red dagger (†).

**Table 1. Summary of zinc titanate films formed from zinc acetate (ZA) and titanium isopropoxide (TTIP)<sup>a</sup>**

Precursor Zn:Ti ratio	Mass of ZA/ g	Volume of TTIP / ml	Composition, 20 mm	Composition, 100 mm	Zn metal fraction (expected)/ mol%
1:1	0.2076(1)	0.330(3)	$\text{Zn}_x\text{Ti}_{3-x}\text{O}_{5.5}$	$\text{Zn}_2\text{TiO}_4$ (tetragonal)	41% (50%)
2:1	0.2769(1)	0.220(2)	$\text{Zn}_2\text{TiO}_4$	$\text{Zn}_2\text{TiO}_4$	66% (66%)
3:1	0.3095(1)	0.165(2)	$\text{Zn}_2\text{TiO}_4$ (48%), $\text{ZnTiO}_3$ (49%), ZnO (3%)	ZnO (66%) and $\text{Zn}_2\text{TiO}_4$ (33%)	74% (75%)
4:1	0.3328(1)	0.135(1)	$\text{Zn}_2\text{TiO}_4$ (96%) ZnO (4%)	ZnO	84% (80%)
5:1	0.3438(1)	0.110(1)	$\text{Zn}_2\text{TiO}_4$ (64%), ZnO (36%)	ZnO	89% (83%)

<sup>a</sup>Depositions carried out using AACVD from 40 ml methanol solution at 450 °C and 0.8 Lmin<sup>-1</sup> argon carrier gas flow. Also stated are the compositions the front (20 mm from leading edge) and rear (100 mm) of the film.

accessible surface area of the samples. Samples of the titania films and a piece of uncoated glass, each of approximately 2.2 cm<sup>2</sup> in area, were submerged for 24 hours in 5 ml of  $7.25 \times 10^{-6}$  M methylene blue solution. This was then dried and the absorbed dye extracted in  $1.6 \times 10^{-3}$  M hydrochloric acid solution. The concentration of the dye in the extracted solution was then determined using the Beer-Lambert law from interpolation to a linear calibration curve determined for  $0.05 \times 10^{-6}$  M to  $1 \times 10^{-6}$  M of acidified methylene blue. The dye extraction step was repeated for each sample until no further dye was found to be desorbing. The cumulative dye extracted was then used to determine the accessible area of each sample.

## Results and Discussion

**Zinc titanate thin film formation.** The formation of thin films of zinc titanate was investigated using the AACVD reaction of mixtures of zinc (II) acetate and titanium (IV) isopropoxide in methanol solution. Initial experiments indicated that films formed below 400 °C were amorphous, but at 450 °C crystalline films were formed with Bragg peaks observable in

the diffraction data. Due to this, subsequent depositions were carried out at 450°C. Here we report on five depositions made with varying amounts of the zinc and titanium precursors, such that the molar ratios (Zn:Ti) were approximately 1:1, 2:1, 3:1, 4:1 and 5:1, while the total molar sum of titanium and zinc remained approximately constant at  $2.25 \times 10^{-3}$  moles. These films will be distinguished in the following text by their precursor ratio, *eg.* the 2:1 film. Each film was analyzed using X-ray diffraction at two points, one 20 mm from the leading edge and a second point further down the film at 100 mm from the leading edge, respective to the direction of the precursor flow, and referred to as the front spot and rear spot respectively. These diffraction patterns can be found in Figure 1. The majority of the films were colorless, with only the presence of the iridescent interference fringes common in thin films. The exception was the 1:1 film where the first 30 mm had an unexpected blue tint. A summary of the conditions used for these five films and the results of the XRD analysis can be found in Table 1. Plots of the Rietveld refinement fits used to determine phase fraction can be found in the Supplementary Figures S1-10.

For the 1:1 film, the front spot had a diffraction pattern that could be matched to that of the recently discovered  $Zn_xTi_{3-x}O_{5-\delta}$  composition, which adopts the pseudobrookite structure.<sup>26</sup> Indexing the diffraction pattern collected from our thin film gave lattice parameters of  $a = 3.721(1) \text{ \AA}$ ,  $b = 9.756(2) \text{ \AA}$  and  $c = 10.058(1) \text{ \AA}$  with a cell volume of  $365.1(1) \text{ \AA}^3$ . This compares with a cell volume of  $370 \text{ \AA}^3$  found by Perry *et al.* for  $Zn_xTi_{3-x}O_{5-\delta}$ , for which they determined a specific composition of  $Zn_{0.61}Ti_{2.39}O_{4.94}$  from a combination of TGA, XRF and refinement to diffraction data.<sup>26</sup> Given the atomic site disorder and vacancies already identified in this structure it is likely that the significant decrease in unit cell size observed in our thin film is caused by variation in the metal fraction,  $x$ . In order to confirm this possibility, XPS measurements were carried out on this portion of the 1:1 synthesized film. After a 180 s etch of the surface in order to ensure investigation of the bulk composition, the Zn:Ti ratio was found to be 1:9, giving an estimated composition of  $Zn_{0.3}Ti_{2.7}O_{4.94}$ , assuming  $\delta$  is unchanged. This allows us to determine the titanium oxidation state as +3.4, compared with +3.6 found in the original paper.<sup>26</sup> This lower oxidation state, and therefore higher concentration of  $Ti^{3+}$ , is consistent with the strong blue tint observed in the film, and the reduced unit cell size due to the greater fraction of smaller titanium ions (ionic radii:  $Zn^{2+}$  0.74  $\text{ \AA}$ ,  $Ti^{3+}$  0.67  $\text{ \AA}$  and  $Ti^{4+}$  0.42  $\text{ \AA}$ ).<sup>43</sup> This, therefore, is the first example of the pseudobrookite zinc titanate found as a thin film, and also provides evidence of an extended structural range due to variation in the metal ion ratio, as previously predicted by computational methods.<sup>26</sup>

The diffraction data collected on the rear spot of the 1:1 film could be matched to the tetragonal spinel form of zinc titanate,  $Zn_2TiO_4$ . From this we can see that the front section of the film is relatively titanium-rich and zinc-poor, with the front spot having a metal basis zinc fraction of 10%, while the rear section has a zinc fraction of 66%. It is possible to calculate a rough estimate of the metal ion ratio across the whole substrate if we assume that the diffraction pattern collected 20 mm from the leading edge is representative of the front half of the film while that collected at 100 mm is representative of the rear half. This is obviously a very crude measure, and also assumes that the film mass remains constant as a function of position, but gives a 'snapshot' of the overall film, which can be compared between samples. Calculating this for the 1:1 film gives an approximate average zinc fraction of 41%, similar to the 50% zinc found in the precursor solution

Analysis of the diffraction patterns of the 2:1 film found that both front and rear spots were composed exclusively of cubic  $Zn_2TiO_4$ , and it is reasonable to therefore assume the intervening film sections are also this phase, giving an average film zinc to titanium ratio matching exactly the precursor ratio. For the 3:1 film, modelling the diffraction pattern from the front spot found it to be composed of a mixture of  $Zn_2TiO_4$  (48% by mass),  $ZnTiO_3$  (49%) with a small amount  $ZnO$  (3%). At the rear the film becomes more enriched with zinc, with Rietveld analysis of the diffraction pattern finding 66%  $ZnO$

and 33%  $Zn_2TiO_4$ . The composition of the two spots gives a crude average metal fraction 74% zinc.

Considering the most zinc-rich reactions, the film made with a 4:1 molar ratio of zinc to titanium precursor was found at the front spot to be almost exclusively cubic  $Zn_2TiO_4$  (96%) with a small amount of  $ZnO$  (4%), and again became more zinc-rich at the rear spot where only peaks corresponding to zinc oxide could be found in the diffraction pattern. Overall, the approximate zinc fraction is 84%. For the final deposition condition, using a 5:1 molar ratio of zinc to titanium precursor, the diffraction pattern collected from the spot 20 mm from the leading edge was found by Rietveld refinement to be mixture of cubic  $Zn_2TiO_4$  (64%) and  $ZnO$  (36%), becoming exclusively zinc oxide at the rear measurement spot. This gave a crude average of 89% metal basis zinc fraction for this film.

The XRD analysis carried out indicates that the ratio of zinc to titanium found in the films can be controlled by the ratio in the precursor solution. This is highlighted in the average zinc fraction calculated for each film as the zinc to titanium precursor ratio increases from 1:1 to 5:1. It can also be seen in the increasing presence of more zinc-rich phases - considering the analysis on the front spot of each film, we find the 1:1 film composed of  $Zn_{0.3}Ti_{2.7}O_{4.94}$  where titanium is dominant, but this progresses to a  $Zn_2TiO_4$  and  $ZnO$  mixture for the 5:1 film. This is not an unexpected result, but does show a key advantage of AACVD in that a single solution can be prepared with multiple precursors, and the fraction of each controlled by measurement of mass or volume, with this ratio retained in the aerosol transported to the reactor and reflected in the ultimate film composition. In more conventional CVD, this level of control from multiple vapor phase precursors is much more challenging, or would require use of a single source precursor which would limit the reaction to a single ratio of metal ions. However, we also observe that although the crude film average and compositional trend matched the precursor solution composition, in each film the front spot was titanium-rich, and the rear titanium-poor, relative to the average. This implied that the titanium precursor had a faster diffusion rate to the substrate, or reacted more readily and was consumed at a faster rate, and therefore is present at a lower concentration towards the rear of the film. Such inconsistency is inherent to static CVD coaters and could be alleviated using a dynamic coater.

Here we have shown that is possible to form films exclusively composed of spinel  $Zn_2TiO_4$  or pseudobrookite  $Zn_{0.3}Ti_{2.7}O_{4.94}$ . Crucially for our original hypothesis, we have also shown that it is possible to make films containing a mixture of  $Zn_2TiO_4$  and  $ZnO$ , which will be necessary for the template-free route to porous titania.

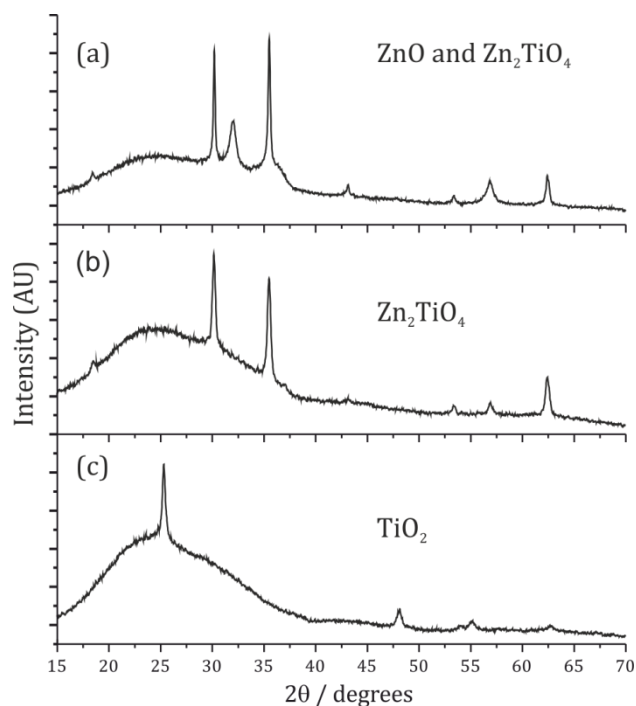


**Figure 2.** (a) Diffraction pattern of the as-made film of ZnO and Zn<sub>2</sub>TiO<sub>4</sub>, (b) pattern after processing with acid showing loss of ZnO, and (c) pattern collected after reduction, showing conversion to TiO<sub>2</sub>.

### Conversion to porous and hierarchically porous TiO<sub>2</sub>.

For the method of forming hierarchically porous titania outlined by Seshadri *et al.*,<sup>21</sup> it was identified that a sample composed 3:1 ZnO to Zn<sub>2</sub>TiO<sub>4</sub>, approximately 50% by mass of each, would allow the formation of a suitable macroporous network after acid removal of the zinc oxide. As discussed above, our thin film made with a zinc acetate to titanium isopropoxide precursor ratio of 4:1 was found to be composed of Zn<sub>2</sub>TiO<sub>4</sub> at the leading edge, shifting to ZnO exclusively at the point 100 mm from the leading edge. Further investigation of this film, at steps of 20 mm along the substrate, found that there was an incremental change in the composition with the section 80 mm from the leading edge having the closest composition to the target with ~40% zinc oxide by mass. A section of the film (25 x 20 mm<sup>2</sup>) centered on this spot was processed with acid to remove the zinc oxide, and then reduced under flowing H<sub>2</sub>/N<sub>2</sub> at 575 °C. Small sections at each stage were retained for SEM imaging, and the progress of the reaction was monitored using XRD. These diffraction patterns can be seen in Figure 2, showing the loss of peaks associated with ZnO after acid leaching, and then conversion of the remaining Zn<sub>2</sub>TiO<sub>4</sub> to the anatase phase of TiO<sub>2</sub>.

Previous work on powders concluded from thermogravimetric analysis that loss of zinc begins at approximately 630 °C, when measured at a rate of 1 K min<sup>-1</sup>, and complete conversion to TiO<sub>2</sub> was achieved by reaction at 752 °C for 12 hours, however at this temperature the rutile polymorph was formed.<sup>21</sup> Here we demonstrate conversion to TiO<sub>2</sub> at a lower temperature, 575 °C, but require considerably

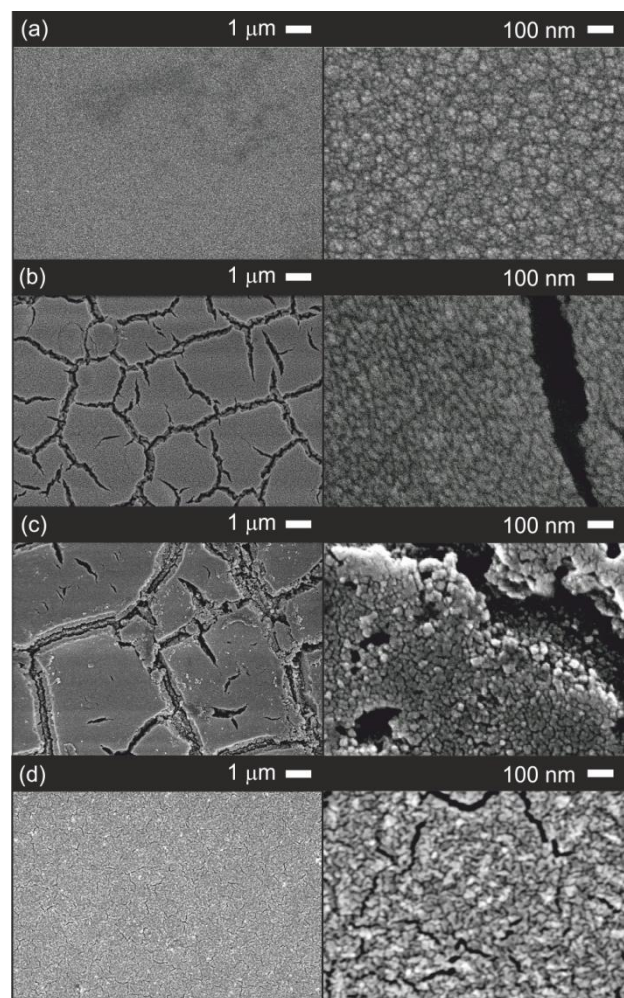


**Figure 3.** SEM images of (a) the as made Zn<sub>2</sub>TiO<sub>4</sub> and ZnO film, (b) after processing with acid to remove ZnO and (c) final HP-TiO<sub>2</sub> after reduction with H<sub>2</sub>/N<sub>2</sub> gas at elevated temperature. Image (d) shows the results of reduction to TiO<sub>2</sub> of a pure Zn<sub>2</sub>TiO<sub>4</sub> film.

longer reaction times of 72 hours. Monitoring at 12, 24 and 48 hours found the conversion to be incomplete. The lower temperature provides an additional advantage, in that the polymorph obtained in our thin film is anatase rather than rutile, and the former is generally considered the more effective photocatalyst.<sup>44</sup>

The SEM image in Figure 3(a) shows that the as-made film of ZnO-Zn<sub>2</sub>TiO<sub>4</sub> has a smooth and continuous surface made of densely packed particles of approximately 50 nm in diameter. Acid etching introduced a network of fissures between the densely packed plates of the remaining Zn<sub>2</sub>TiO<sub>4</sub> as shown in Figure 3(b). The final stage of hydrogen reduction can then be seen in Figure 3(c) to have introduced much finer porosity – pores less than 10 nm in size – within the formerly dense plates, alongside the larger fissures which are 200-500 nm in diameter. A side-on image of this film can be found in the supporting information. It is clear from the SEM and XRD evidence that the processing of the ZnO-Zn<sub>2</sub>TiO<sub>4</sub> film has successfully

converted it to a film of hierarchically porous TiO<sub>2</sub>, referred to hence as *HP-TiO<sub>2</sub>*.

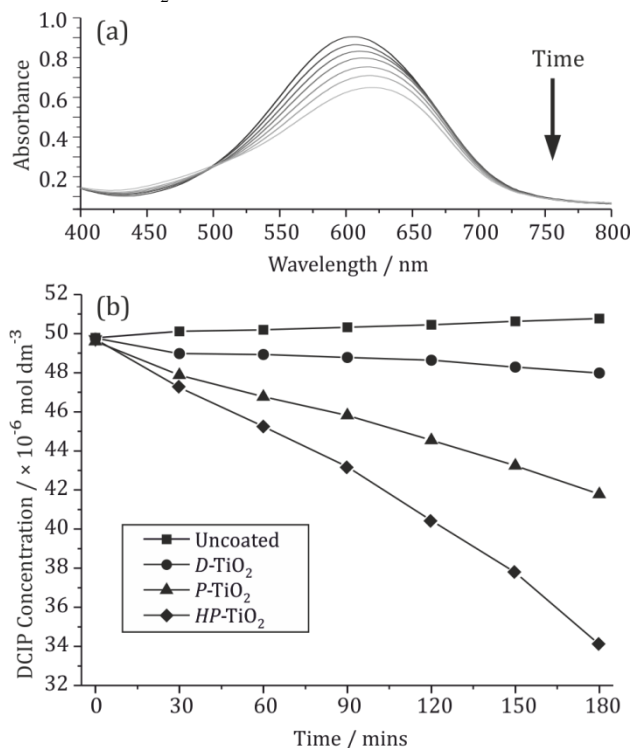


**Figure 4.** (a) Example data set of visible spectra recorded on dye solution aliquots taken after exposure to UV and *HP-TiO<sub>2</sub>* photocatalyst, recorded at 30 min intervals, showing clear reduction in peak intensity with time. (b) Values of dye concentration as a function of time for the three titania samples and an uncoated control.

For comparison to the *HP-TiO<sub>2</sub>* film, a section of Zn<sub>2</sub>TiO<sub>4</sub> film without any zinc oxide was taken from the front of the 4:1 film, centered around the spot 20 mm from the leading edge. This was also processed using flowing H<sub>2</sub>/N<sub>2</sub> at 575 °C and the X-ray diffraction pattern again showed the conversion of this to anatase TiO<sub>2</sub>. The SEM images in Figure 3(d) show the presence of small scale pores of approximately 20 nm in diameter, induced by the decomposition of zinc titanate, but no larger scale fissures as in the *HP-TiO<sub>2</sub>* sample. As this sample contained only the small scale pores, it will be referred to as porous titania or *P-TiO<sub>2</sub>* and will be used to compare the effect of a single scale of porosity against the hierarchical porosity observed in *HP-TiO<sub>2</sub>*.

A control film of titanium dioxide was also synthesized directly using AACVD from 2.25 × 10<sup>-3</sup> moles of titanium isopropoxide at 450 °C. XRD confirmed the formation of a film of anatase TiO<sub>2</sub>. This was used for comparison to the two porous samples of titania, and will be referred to as the dense titania film or *D-TiO<sub>2</sub>* film. Diffraction patterns for *P-TiO<sub>2</sub>* and *D-TiO<sub>2</sub>* can be found in the Supporting Information, figure S12.

**Photocatalytic activity of porous titania.** The three titania film samples, *HP-TiO<sub>2</sub>*, *P-TiO<sub>2</sub>*, and *D-TiO<sub>2</sub>*, were assessed for photocatalytic activity, along with an uncoated piece of glass, using two tests; dye decolouration and stearic acid degradation.

**Table 2.** Summary of the photocatalytic rates of the dye decolouration and stearic acid decomposition tests for the three titania samples.<sup>a</sup>

Photocatalytic test	<i>D-TiO<sub>2</sub></i>	<i>P-TiO<sub>2</sub></i>	<i>HP-TiO<sub>2</sub></i>
Dye 0 <sup>th</sup> order rate / × 10 <sup>-9</sup> mol dm <sup>-3</sup> min <sup>-1</sup> cm <sup>-2</sup>	1.76(7)	7.1(3)	21.7(9)
Dye FQE / × 10 <sup>-4</sup> molecules photon <sup>-1</sup>	0.61(2)	2.4(1)	7.5(3)
Dye rate relative to <i>D-TiO<sub>2</sub></i>	1.00(4)	4.0(2)	12.3(5)
Stearic Acid 0 <sup>th</sup> order rate / × 10 <sup>13</sup> molecules min <sup>-1</sup> cm <sup>-2</sup>	3.0(4)	9.6(9)	43(2)
Stearic Acid FQE / × 10 <sup>-4</sup> molecules photon <sup>-1</sup>	0.48(6)	1.6(1)	7.0(3)
Stearic acid rate relative to <i>D-TiO<sub>2</sub></i>	1.0(1)	3.3(3)	14.4(7)
Accessible surface area ratio	2.8(2)	7.1(4)	32(2)
Surface area relative to <i>D-TiO<sub>2</sub></i>	1.00(6)	2.5(2)	11.4(6)

<sup>a</sup>Values given in molar units, as formal quantum efficiencies (FQEs), and as ratios relative to the non-porous *D-TiO<sub>2</sub>* sample. The table also includes the accessible surface area measurements, conducted using methylene blue dye, as the ratio of dye accessible area to apparent surface area.

In the dye decolouration test the samples were individually submerged in a solution of dichloroindophenol (DCIP) dye and glycerol. Under UV light irradiation the TiO<sub>2</sub> photocatalyst can reduce the dye, converting it from a blue to a colorless form, with the progress of this reaction monitored using visible light spectroscopy. An example set of spectra showing the decrease in absorption of the dye at 30 minute intervals are shown in Figure 4(a) for the experiment conducted with *HP-TiO<sub>2</sub>*. The Beer-Lambert law was used to calculate the concentration of the dye in the solution, based on a measured extinction coefficient for DCIP of  $\epsilon_{606\text{nm}} = 1.64 \times 10^4 \text{ cm}^{-1}$ . The dye concentration for each of the samples tested as a function of time is shown in Figure 4(b). This shows that for the uncoated control there is no decrease in DCIP concentration from UV light exposure alone, and in fact the dye concentration increases with time. This is not an artefact of the measurement, but a real effect due to evaporation of a small fraction of the solvent over the course of the experiment - approximately 0.45 ml from the 25 ml test solution. The increase in concentration this causes, as highlighted by the blank control, means that rates of dye degradation for the coated samples reported below are underestimates of the true rates by approximately 2% - although this falls within the error of the measurements.

If taken to completion, it has been shown that photocatalytic dye decolouration proceeds *via* Langmuir-Hinshelwood kinetics - where overall 1<sup>st</sup> order kinetics would be expected when dye diffusion is the limiting factor.<sup>45</sup> Our data instead indicate initial zero order kinetics, which is expected when the substrate is saturated with dye.<sup>40</sup> We achieved this by allowing the system to reach equilibrium before initiating the photocatalytic reaction, and it was confirmed by an initial drop in dye concentration for all samples after 30 mins stirring to approximately 5.00 × 10<sup>-5</sup> mol dm<sup>-3</sup> compared to the stock dye solution at 5.22 × 10<sup>-5</sup> mol dm<sup>-3</sup>. These initial, zero order degradation rates can be found in Table 2. They show that relative to the non-porous *D-TiO<sub>2</sub>*, the porous *P-TiO<sub>2</sub>* sample

had a rate 4.0(2) times higher, while the rate for the *HP*-TiO<sub>2</sub> film was increased by greater than an order of magnitude to

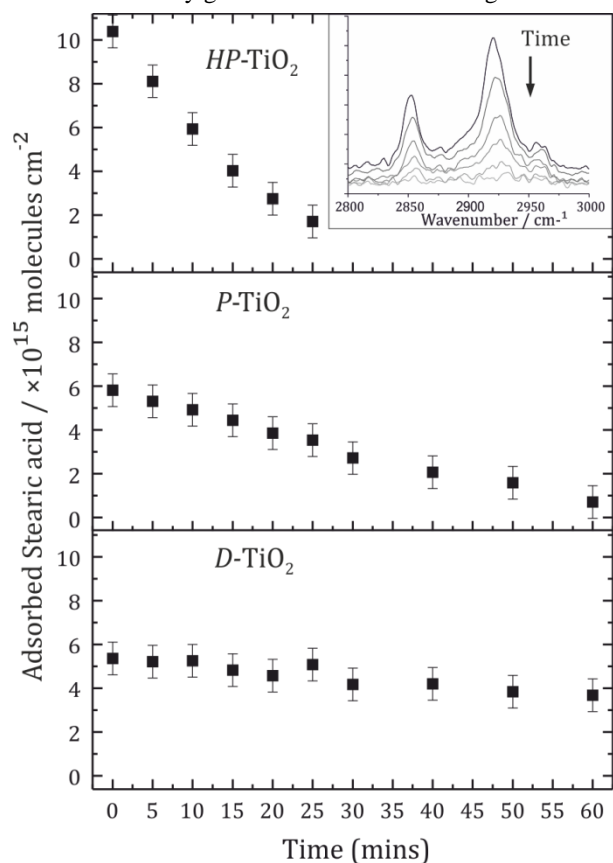


**Figure 5.** Plots of adsorbed stearic acid as a function of irradiation time, for the three samples, *HP*-TiO<sub>2</sub>, *P*-TiO<sub>2</sub>, and *D*-TiO<sub>2</sub>. Top inset shows the FTIR data for *HP*-TiO<sub>2</sub>.

12.3(5) times faster. These are significant increases in photocatalytic activity through the introduction of porosity.

In the second photocatalytic test a layer of stearic acid was dip coated onto the surface of the samples, and then the stearic acid degradation under 365 nm UV light monitored using FTIR. Example data are shown in the Figure 5 inset. Each sample was masked such that the exposed test surface was 0.78 cm<sup>2</sup>. The area under the peaks in the FTIR was integrated and converted into the number of moles of stearic acid. The data for each sample as a function of time can be seen in Figure 5. The uncoated control is not included, as this showed no change in stearic acid loading across the 60 mins of UV exposure, within the margin of error.

In Figure 5 it can be seen that despite identical dip coating parameters, the three samples do not have the same loading of stearic acid. The *P*-TiO<sub>2</sub> film has a slightly higher stearic acid loading than *D*-TiO<sub>2</sub> sample with  $5.8(7) \times 10^{15}$  molecules cm<sup>-2</sup> compared to  $5.4(7) \times 10^{15}$  molecules cm<sup>-2</sup>, but the *HP*-TiO<sub>2</sub> sample has a value almost twice this at  $10.4(7) \times 10^{15}$  molecules cm<sup>-2</sup>. This is indicative of the high accessible surface area and increased porosity of this sample. A similar effect was not observed during the dye degradation test because the

amount of dye absorbed was much smaller than the dye remaining in solution, with which it was in equilibrium.

For complete degradation of stearic acid films, the kinetics have been shown to be first order,<sup>1</sup> but results are most often reported in terms of the initial pseudo-zero order rate, measured in molecules min<sup>-1</sup> cm<sup>-2</sup>, or to take account of different light intensities, as the formal quantum efficiency (FQE) - the ratio of rate of removal of stearic acid to rate of incident light (molecules photon<sup>-1</sup>). Both values are given for our samples in Table 2. For the *D*-TiO<sub>2</sub> we found an FQE of  $0.48(6) \times 10^{-4}$ , increasing to  $1.6(1) \times 10^{-4}$  for *P*-TiO<sub>2</sub> and  $7.0(3) \times 10^{-4}$  for *HP*-TiO<sub>2</sub>, once again observing over an order of magnitude increase in activity for the hierarchically porous sample compared to the dense control film. The stearic acid degradation test is widely used, and the relative simplicity of the experimental set up make values between different authors more comparable than the DCIP decolouration test. Under 365 nm UV illumination previously reported FQE values for stearic acid degradation for TiO<sub>2</sub> thin films are typically found between  $0.14 \times 10^{-4}$  and  $1.25 \times 10^{-4}$  molecules photon<sup>-1</sup>, a range which our control *D*-TiO<sub>2</sub> falls within, but is exceeded by both the *P*- and *HP*-TiO<sub>2</sub> samples.<sup>46-49</sup> Higher values have been reported for films composed of powder particles, which are likely due to higher surface area; for example  $10.9 \times 10^{-4}$  molecules photon<sup>-1</sup> for a powder film produced using liquid flame spray.<sup>50</sup> The highest FQE results are often found to have been collected using a larger initial loading of stearic acid, which can artificially inflate the initial FQE values as the true kinetics are first order, and also using lower intensity light which can also affect the FQE as photocatalytic rates are not linear with light intensity.<sup>51</sup> In order to provide a fair comparison to these results we carried out a further experiment with the *HP*-TiO<sub>2</sub> sample, using a lower intensity UV lamp, measured at 1.1 mWcm<sup>-2</sup>, and a higher initial stearic acid loading of  $3.51(7) \times 10^{15}$  molecules cm<sup>-2</sup>. We found for that under these conditions our hierarchically porous sample had an FQE of  $18(1) \times 10^{-4}$ , which to our knowledge is the highest yet reported for a TiO<sub>2</sub> film.

**Accessible Surface Area.** Dye absorption was used to determine the accessible surface areas of each film.<sup>52-53</sup> Samples of the titania films and a piece of uncoated glass were submerged in methylene blue solution, dried and then the absorbed dye extracted using dilute acid. Dye extraction from the samples was repeated until no further dye could be extracted. The concentration of the methylene blue dye in this extracted solution was then determined using the Beer-Lambert law and a calibration curve. The calibration curve was produced with seven samples of acidified methylene blue solution ranging in concentration from  $0.5 \times 10^{-7}$  M to  $10 \times 10^{-7}$  M, and was found to be linear in this region, with a regression R<sup>2</sup> of 0.998. The extracted dye solutions were all found to fall within this range, allowing us to interpolate from the calibration data.

Our uncoated control substrate had a total measured surface area of 5.38(7) cm<sup>2</sup>, which was able to absorb a total of  $5.1(1) \times 10^{10}$  moles of methylene blue dye. From this we could estimate the area occupied per molecule of dye as 1.76(3) nm<sup>2</sup>,

comparable with previous work on clays where a value of 1.3 nm<sup>2</sup> was determined.<sup>53</sup> For our thin films the experimental

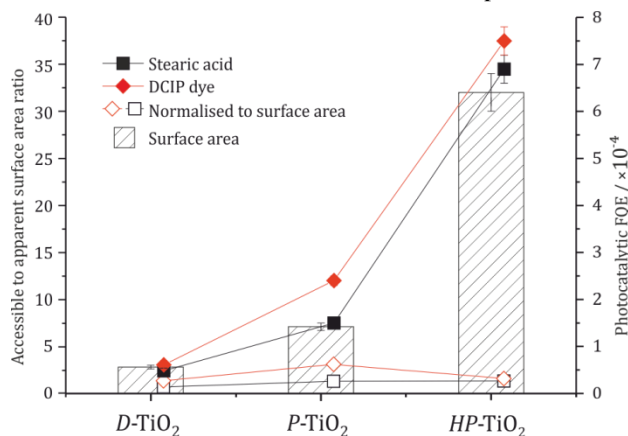


Figure 6. Bar chart displays the surface area of the three titania samples, with the scale to the left. Superimposed are photocatalytic formal quantum efficiencies (FQEs) of stearic acid degradation (squares) and DCIP dye decolouration (diamonds), with scale to the right. The filled markers show the actual FQE, the empty symbols are the values normalized to accessible surface area. Where they cannot be observed, error bars are smaller than the markers, and the lines are guides to the eye only.

value was used to convert the total absorbed dye for each sample into an accessible surface area, from which the surface area of the uncoated rear and sides of the substrate was subtracted, leaving the accessible surface area within the coating itself. The most meaningful expression for this surface area is the ratio of the accessible surface area to the apparent coated area, similar to the roughness factor. For the *D*-TiO<sub>2</sub> sample an absorbed dye surface area of 6.8(3) cm<sup>2</sup> was found for a coated film area of 2.5(1) cm<sup>2</sup>, giving an accessible surface area ratio of 2.8(2) times greater than the apparent surface area of the coating. This indicates that, as expected, the surface of the titania film is considerably rougher than the uncoated glass. The *P*-TiO<sub>2</sub> sample had a ratio of 7.1(4) while this increases to 32(2) for the *HP*-TiO<sub>2</sub>, confirming the large increase in surface area expected from the SEM imaging and increase in photocatalytic activity.

Both of the photocatalytic tests - the dye decolourisation and stearic acid degradation - show that the *HP*-TiO<sub>2</sub> sample has over an order of magnitude increase in activity compared to the dense non-porous control. The accessible surface area evidence suggests, however, that this increase originates only from the much larger surface area of the photocatalyst, as can be seen in Figure 6, where the FQE values of both tests are normalized to the surface area. This shows that there is almost no difference in photocatalytic rates for all three samples, in either test. We therefore observe no synergetic effect of having multi-scale porosity, matching the results previously seen by Caruso *et al.*<sup>15</sup> Nonetheless, the absolute increases in activity we have observed, factors of 12 and 14 over conventional films, indicate that this is a facile but highly valuable approach to increasing photocatalytic activity in thin films.

## Conclusions

We have shown that zinc acetate and titanium isopropoxide are viable precursors for the formation of zinc titanate and mixed zinc titanate-zinc oxide thin films. The use of these precursors in methanol solution allows deposition of films where the ratio of the two precursors can allow selective deposition of specific zinc titanate phases with controlled zinc to titanium ratios.

We have also confirmed that conversion of mixed films of zinc titanate and zinc oxide to titanium dioxide through etching and vapor phase reduction leads to the formation of hierarchically structured films of titania with significant increases in accessible surface area. Although we observe no synergistic increase in photocatalytic activity due to the hierarchical porosity, the much higher surface area of this material allowed us to observe an increase in photocatalytic activity of up to 14 times greater than an equivalent non-porous titania film. For the stearic acid degradation test carried out with this sample, we report what we believe to be the highest FQE for a TiO<sub>2</sub> film yet found using 365 nm UV light, with a value of 18(1) × 10<sup>-4</sup> molecules photon<sup>-1</sup>. We can therefore conclude that the synthetic method reported here is an effective template-free route to the formation of highly porous titanium dioxide films, that can be used to maximize the potential of titania in self-cleaning and pollution remediation applications.

## Acknowledgements

The authors thank the EPSRC for funding through grant reference EP/K039466/1. We also wish to thank the Royal Society for research funds.

## Notes and references

<sup>a</sup> Department of Chemistry, University of Southampton, Southampton, SO17 1BJ, United Kingdom

<sup>b</sup> School of Chemistry, University of Leeds, Leeds, LS2 9J, United Kingdom

<sup>c</sup> Christopher Ingold Laboratories, UCL, 20 Gordon Street, London, WC1H 0AJ, United Kingdom

Electronic Supplementary Information (ESI) available: Figures S1 to S10 show the X-ray diffraction pattern and Rietveld fits for the zinc titanate thin films. Figure S11 shows the diffraction patterns for *P*-TiO<sub>2</sub> and *D*-TiO<sub>2</sub> samples. See DOI for the supporting information, and also for the raw data used in preparation of this manuscript:

1. A. Mills, A. Lepre, N. Elliott, S. Bhopal, I. P. Parkin and S. A. O'Neill, *J. Photochem. Photobiol., A*, 2003, **160**, 213-224.
2. A. Mills, R. H. Davies and D. Worsley, *Chem. Soc. Rev.*, 1993, **22**, 417-425.
3. K. P. Kühn, I. F. Chaberny, K. Massholder, M. Stickler, V. W. Benz, H.-G. Sonntag and L. Erdinger, *Chemosphere*, 2003, **53**, 71-77.

4. Z. A. Aiken, G. Hyett, C. W. Dunnill, M. Wilson, J. Pratten and I. P. Parkin, *Chem. Vap. Deposition*, 2010, **16**, 19-22.
5. A. Mills and S. LeHunte, *J. Photochem. Photobiol., A*, 1997, **108**, 1-35.
6. M. Mehrvar, W. A. Anderson and M. Moo-Young, *Advances in Environmental Research*, 2002, **6**, 411-418.
7. A. E. Cassano and O. M. Alfano, *Catal. Today*, 2000, **58**, 167-197.
8. O. M. Alfano, D. Bahnemann, A. E. Cassano, R. Dillert and R. Goslich, *Catal. Today*, 2000, **58**, 199-230.
9. X. Li, H. Wang, K. Inoue, M. Uehara, H. Nakamura, M. Miyazaki, E. Abe and H. Maeda, *Chem. Commun.*, 2003, DOI: 10.1039/B300765K, 964-965.
10. A. Mills and S. Elouali, *J. Photochem. Photobiol., A*, 2015, **305**, 29-36.
11. Y. Ohko, Y. Nakamura, N. Negishi, S. Matsuzawa and K. Takeuchi, *J. Photochem. Photobiol., A*, 2009, **205**, 28-33.
12. Z. Xing, W. Zhou, F. Du, L. Zhang, Z. Li, H. Zhang and W. Li, *ACS Applied Materials & Interfaces*, 2014, DOI: 10.1021/am5034236, 16653-16660.
13. H. Zeng, J. Xie, H. Xie, B.-L. Su, M. Wang, H. Ping, W. Wang, H. Wang and Z. Fu, *Journal of Materials Chemistry A*, 2015, DOI: 10.1039/C5TA04649A, 19588-19596.
14. G. L. Drisko, A. Zelcer, V. Luca, R. A. Caruso and G. J. d. A. A. Soler-Illia, *Chem. Mater.*, 2010, **22**, 4379-4385.
15. N. M. Nursam, X. Wang and R. A. Caruso, *Journal of Materials Chemistry A*, 2015, **3**, 24557-24567.
16. P. Trogadas, V. Ramani, P. Strasser, T. F. Fuller and M.-O. Coppens, *Angew. Chem. Int. Edit.*, 2016, **55**, 122-148.
17. S. J. Bu, Z. G. Jin, X. X. Liu, L. R. Yang and Z. J. Cheng, *J. Eur. Ceram. Soc.*, 2005, **25**, 673-679.
18. J. Li, P. Lommens, E. Bruneel and I. Van Driessche, *J. Mater. Sci.*, 2012, **47**, 6366-6374.
19. E. S. Toberer and R. Seshadri, *Chem. Commun.*, 2006, 3159-3165.
20. C. Lermer, M. M. Butala, B. R. Lettiere and R. Seshadri, *Cryst. Growth Des.*, 2014, **14**, 4526-4530.
21. E. S. Toberer, J. D. Epping, B. F. Chmelka and R. Seshadri, *Chem. Mater.*, 2006, **18**, 6345-6351.
22. K. Choy, *Prog. Mater. Sci.* **2003**, **48**, 57-170.
23. R. L. Millard, R. C. Peterson and B. K. Hunter, *Am. Mineral.*, 1995, **80**, 885-896.
24. S. F. Bartram and R. A. Slepetyts, *J. Am. Ceram. Soc.*, 1961, **44**, 493-499.
25. S. Takai, T. Shinohara, A. Hoshikawa, S. Harjo, K. Oikawa, T. Ishigaki, T. Kamiyama and T. Esaka, *J. Ceram. Soc. Jpn.*, 2007, **115**, 780-785.
26. N. H. Perry, V. Stevanovic, L. Y. Lim and T. O. Mason, *Dalton Trans.*, 2016, **45**, 1572-1581.
27. S.-C. Wu, Y.-R. Jeng, W.-H. Yau, K.-T. Wu, C.-H. Tsai and C.-P. Chou, *Appl. Surf. Sci.*, 2012, **258**, 6730-6734.
28. S. J. Zhang, M. S. Li, S. L. Feng and C. Cao, *Adv. Mater. Res. (Durnten-Zurich, Switz.)*, 2014, **900**, 415-418, 415 pp.
29. Y.-S. Chang, Y.-H. Chang, I.-G. Chen, G.-J. Chen and Y.-L. Chai, *J. Cryst. Growth*, 2002, **243**, 319-326.
30. K. Sarkar, E. V. Braden, T. Froeschl, N. Huesing and P. Mueller-Buschbaum, *J. Mater. Chem. A*, 2014, **2**, 15008-15014.
31. F. A. Hernandez-Garcia, G. Torres-Delgado, R. Castanedo-Perez and O. Zelaya-Angel, *Environ. Sci. Pollut. Res.*, 2016, **23**, 13191-13199.
32. S. A. Mayen-Hernandez, G. Torres-Delgado, R. Castanedo-Perez, J. Marquez Marin, M. Gutierrez-Villarreal and O. Zelaya-Angel, *Sol. Energy Mater. Sol. Cells*, 2007, **91**, 1454-1457.
33. Z.-X. Chen, J. van der Eyden, W. Koot, R. van den Berg, J. v. Mechelen and A. Derking, *J. Am. Ceram. Soc.*, 1995, **78**, 2993-3001.
34. P. Marchand, I. A. Hassan, I. P. Parkin and C. J. Carmalt, *Dalton Trans.*, 2013, **42**, 9406-9422.
35. M. R. Waugh, G. Hyett and I. P. Parkin, *Chem. Vap. Deposition*, 2008, **14**, 366-372.
36. C. Edusi, G. Hyett, G. Sankar and I. P. Parkin, *Chem. Vap. Deposition*, 2011, **17**, 30-36.
37. A. C. Larson and R. B. Von Dreele, *Los Alamos National Laboratory Report LAUR*, 2000, 86-748.
38. B. H. Toby, *J. Appl. Crystallogr.*, 2001, **34**, 210-213.
39. G. Hyett, M. Green and I. P. Parkin, *J. Am. Chem. Soc.*, 2006, **128**, 12147-12155.
40. A. Mills and M. McGrady, *J. Photochem. Photobiol., A*, 2008, **193**, 228-236.
41. P. Sawunyama, L. Jiang, A. Fujishima and K. Hashimoto, *J. Phys. Chem. B*, 1997, **101**, 11000-11003.
42. A. Mills and J. Wang, *J. Photochem. Photobiol., A*, 2006, **182**, 181-186.
43. R. D. Shannon, *Acta Crystallographica Section A*, 1976, **32**, 751-767.
44. G. Li and K. A. Gray, *Chem. Phys.*, 2007, **339**, 173-187.
45. A. Mills, J. Wang and M. McGrady, *J. Phys. Chem. B*, 2006, **110**, 18324-18331.
46. R. Quesada-Cabrera, C. Sotelo-Vazquez, J. A. Darr and I. P. Parkin, *Applied Catalysis B: Environmental*, 2014, **160-161**, 582-588.
47. J. S. Park and W. Choi, *Langmuir*, 2004, **20**, 11523-11527.
48. V. Pore, A. Rahtu, M. Leskelä, M. Ritala, T. Sajavaara and J. Keinonen, *Chem. Vap. Deposition*, 2004, **10**, 143-148.
49. A. Kafizas, C. W. Dunnill and I. P. Parkin, *Phys. Chem. Chem. Phys.*, 2011, **13**, 13827-13838.
50. H. Keskinen, J. M. Mäkelä, M. Aromaa, J. Keskinen, S. Areva, C. V. Teixeira, J. B. Rosenholm, V. Pore, M. Ritala, M. Leskelä, M. Raulio, M. S. Salkinoja-Salonen, E. Levänen and T. Mäntylä, *Catal. Lett.*, 2006, **111**, 127-132.
51. R. Quesada-Cabrera, A. Mills and C. O'Rourke, *Applied Catalysis B: Environmental*, 2014, **150-151**, 338-344.
52. S. Xu and S. A. Boyd, *Langmuir*, 1995, **11**, 2508-2514.
53. G. Chen, J. Pan, B. Han and H. Yan, *J. Dispersion Sci. Technol.*, 1999, **20**, 1179-1187.